Geophysical Journal International

Crustal and uppermost mantle structure of the NW Namibia continental margin and the Walvis Ridge derived from ambient seismic noise

T. Ryberg [1], W. H. Geissler,[2] W. Jokat [2,3] X. Yuan [1] T. Fromm,[2] S. Pandey[2,4] and B. Heit[1]

[1]*Helmholtz Centre Potsdam GFZ German Research Centre for Geosciences, Telegrafenberg, Potsdam, Telegrafenberg,* 14473 *Potsdam, Germany. Email:* *trond@gfz-potsdam.de*
[2]*Alfred Wegener Institute Helmholtz Centre for Polar and Marine Research, Am Handelshafen* 12, 27570 *Bremerhaven, Germany*
[3]*University of Bremen, Department of Geoscience,* 28359 *Bremen, Germany*
[4]*Shillong Geophysical Research Centre, IIG, Wilton Hall Estate, Upper Shillong* 793005, *India*

SUMMARY

The Walvis Ridge (WR) is the most prominent hotspot track related to the opening in the South Atlantic Ocean. Several hypotheses have been developed to explain its origin and evolution. The presence of a massive magmatic structure at the landfall of the WR in Northwest Namibia raised speculation about the role of a hotspot during the opening of the South Atlantic ocean. To investigate its deeper velocity structure at the junction of the WR with the African continent was the focus of the amphibious seismological WALPASS experiment. In total 12 ocean-bottom seismometers and 28 broad-band land stations were installed between 2010 and 2012 to acquire seismological data. Here, we present the results of seismic ambient noise tomography to investigate to which extent the Tristan hotspot modified the crustal structure in the landward prolongation of the ridge and in the adjacent oceanic basins. For the tomography, vertical and hydrophone component cross correlations for >300 d for OBS stations and between 1 and 2 yr for land stations data were analysed. More than 49 000 velocity measurements (742 dispersion curves) were inverted for group velocity maps at 75 individual signal periods, which then had been inverted for a regional 3-D shear wave velocity model. The resulting 3-D model reveals structural features of the crust related to the continent–ocean transition and its disturbance caused by the initial formation of the WR ∼130 Ma. We found relatively thick continental crust below Northwest Namibia and below the near-shore part of the WR, a strong asymmetry offshore with typical, thin oceanic crust in the Namibe Basin (crossing over into the Angola Basin further offshore) to the North and a wide zone of transitional crust towards the Walvis Basin south of the WR.

Key words: Composition and structure of the oceanic crust; Tomography; Crustal imaging; Seismic interferometry; Surface waves and free oscillations; Continental margins: divergent.

1 INTRODUCTION

Mantle plumes rising from the core–mantle boundary deliver excess materials to form the hotspot trails on the oceanic floor in the form of volcanic ridges or seamount chains. In this study a prominent magmatic ridge in the South Atlantic, the Walvis Ridge (WR), has been investigated to constrain its crustal structure at the junction with the continent. Knowledge of the crustal fabric in this continent–ocean transition area can provide an estimate on the amount of the igneous material building the ridge and the imprints of the mantle plume. In the last two decades, this region has been investigated by controlled-source seismic experiments (Bauer *et al.* 2000, 2003) and global teleseismic studies (Ritsema & Allen 2003; Sebai *et al.* 2006) unravelling velocity variations in the upper mantle of the eastern South Atlantic Ocean, which might have been caused by a Cretaceous mantle plume (Sebai *et al.* 2006; Colli *et al.* 2013). Seismic wide-angle reflection and refraction data aimed also to image the 2-D crustal structure (Fromm *et al.* 2015) at the junction of the WR with the Namibian coast. These data did not provide evidence for large-scale intrusions and magmatic modification within the continental crust in NW Namibia. However,
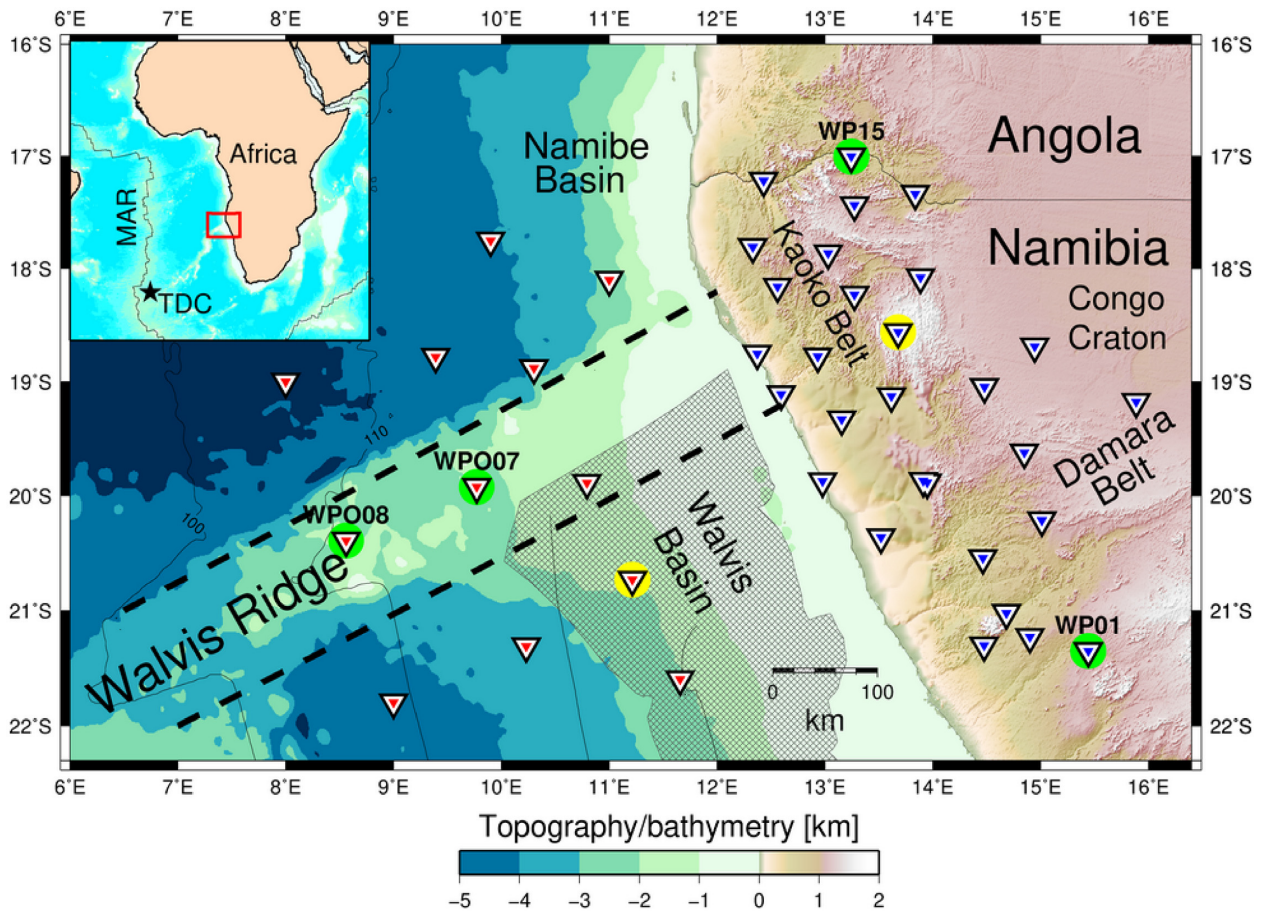
Figure 1. Map of the study region showing the network location of 12 ocean bottom seismic broad-band stations (red triangles) around the Walvis Ridge and 28 broad-band land stations in Northern Namibia (blue triangles). Seafloor ages are from Müller *et al.* (2008). The hashed area shows the region where SDRs (seaward-dipping reflectors) occur (Koopmann *et al.* 2014b). Dashed lines indicate the extent of the Walvis Ridge. MAR, Mid-Atlantic Ridge; TDC, Tristan da Cunha hotspot. Triangles encircled in green show the locations of station pairs for which dispersion curves are shown (see text). Triangles encircled in yellow show the locations of stations with exemplary dispersion curve inversions.

the set-up was not suitable to reliably identify larger-scale (regional) upper mantle anomalies at the base of the continental crust that could be indicative of a long-lasting large plume head–lithosphere interaction.

Thus, our study area includes parts of the Congo Craton, the Damara mobile belt south of it and the Kaoko mobile belt along the coast (Schneider *et al.* 2008; Khoza *et al.* 2013, and references therein). These units formed part of Gondwana prior to the opening of the South Atlantic in the early Cretaceous ∼130 Ma (Heine *et al.* 2013). Our amphibious experimental set-up was designed to close the knowledge gap by deriving a 3-D model of the *S*-wave velocity structure at the WR landfall by using ambient noise tomography. During the last decades, interferometric methods of seismic imaging based on ambient noise have been developed. These methods (called ambient noise tomography or ANT) are based on the analysis of surface waves recovered by cross correlations of ubiquitous ambient noise recorded at station pairs (Sabra *et al.* 2005; Shapiro *et al.* 2005; Bensen *et al.* 2007). With group velocity dispersion curves between periods from a few to ∼40 s using the ANT it is possible to constrain the 3-D *S*-wave velocity structure of the crust and the uppermost mantle by a combination of tomographic and surface wave inversion methods (two-step inversion). Applying these methods will provide qualitative insights on how much a plume head modified the continental crust/lithosphere in the early phase of continental breakup at the junction of the WR with the NW Namibian coast.

2 DATA ACQUISITION AND PROCESSING

The seismological network consisting of 12 ocean-bottom seismometers (OBS) and 28 land stations covers an area of ∼800 km by ∼500 km (Fig. 1). The onshore network was in operation between November 2010 and November 2012, the offshore part recorded data in 2011 (Heit *et al.* 2010). Both subnetworks were equipped with various Güralp broad-band sensors (CMG-40T, CMG-3ESP/60, CMG-3T/100 for the land stations, CMG-40T/30 for the OBS stations). The data (vertical and hydrophone components) were restituted accordingly, decimated to 5 samples per second and split into daily segments for further processing. Continuous records of typically 350 d for OBS and between 350 and 700 d for land stations were available for the ambient noise analysis, respectively.
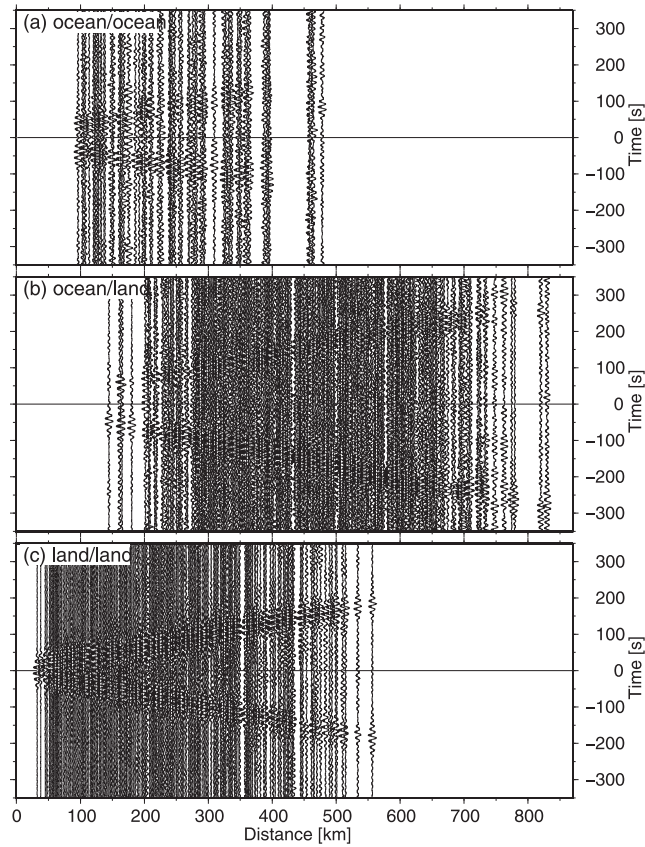
Figure 2. Record sections of the cross correlation data (EGF) of all vertical-component ocean station (a), land/ocean station (b) and land station (c) pairs, bandpassed between 10 and 20 s signal period. Traces are normalized. The coherent phase is dominated by the signal of ∼15 s period, corresponding to Rayleigh waves travelling in the crust with a group velocity of ∼3.1 km s⁻¹.

By combining ambient noise techniques, dispersion curve analysis of Rayleigh waves, 2-D tomographic inversion of traveltimes and 1-D depth inversion of dispersion curve data we derived an amphibious 3-D *Vs* model. While most of the ANT studies focus on continental structures, only a few involve ocean bottom seismographs or amphibious seismic instrumentation targeting marine structures and/or transitions into the continent (Harmon *et al.* 2007; Yao *et al.* 2011; Zha *et al.* 2014; Gao & Shen 2015; Ball *et al.* 2016; Corela *et al.* 2017; Lynner & Porritt 2017; Ryberg *et al.* 2017; Hable *et al.* 2019; Guerin *et al.* 2020; Feng 2021; Li *et al.* 2021; Wolf *et al.* 2021; Yamaya *et al.* 2021). We follow the method described by Ryberg *et al.* (2016b, 2017) to derive fundamental mode Rayleigh waves between station pairs from ambient seismic noise (Campillo & Paul 2003; Shapiro *et al.* 2005; Schuster 2009; Campillo & Roux 2014). The inversion of a final shear wave velocity model is done in two steps: After derivation of the empirical Green's function (EGF), group velocities of the Rayleigh wave phases are determined, 2-D tomographical models (for every signal period) are inverted followed by a 1-D depth inversion using Bayesian Markov-chain Monte Carlo (McMC) inversion method at every grid location.

Data quality of the EGFs can be assessed by plotting a band-passed virtual shot gather (distance–time plot, see Fig. 2). Surface wave phases with good signal-to-noise ratio can be observed over the entire distance range for virtually all station pairs (land–land, ocean–ocean and land–ocean).

From those cross correlations, a dispersion curve analysis was done, resulting in frequency dependent interstation group velocities. Generally, the seismic traces derived from cross correlations are dominated by oceanic microseisms (i.e. Longuet-Higgins 1950). We determined the group velocities of the Rayleigh waves using a multiple-filter, frequency–time technique (Dziewonski *et al.* 1969). Fig. 3(a) shows the result of the frequency–time analysis for the oceanic station pair WPO07–WPO08, dominated by fundamental mode Rayleigh and Scholte waves (Scholte 1947). Examples of dispersion curves for station combinations along land–land and land-oceanic wave paths are shown in Figs 3(b) and (c), respectively.

The traveltimes (or group velocities) had been picked for all available station pairs requiring a minimum of three wavelengths for interstation distance using the *xdcpick* tool (Ryberg *et al.* 2021). We started the manual picking of every trace when an energetic arrival was present at periods ∼15 s (microseisms peak), from there extending the picking to lower and higher periods until a coherent (continuous) dispersion curve branch disappeared. We accepted the dispersion curve if it would span at least one octave. Fig. 4 gives an overview over all derived Rayleigh wave group velocities, separately for land, oceanic and land/oceanic station combinations. For most of the station pairs, dispersion curves in the period range from 1 to ∼40 s could be identified and picked, resulting in 200–800 traveltime picks at every signal frequency.
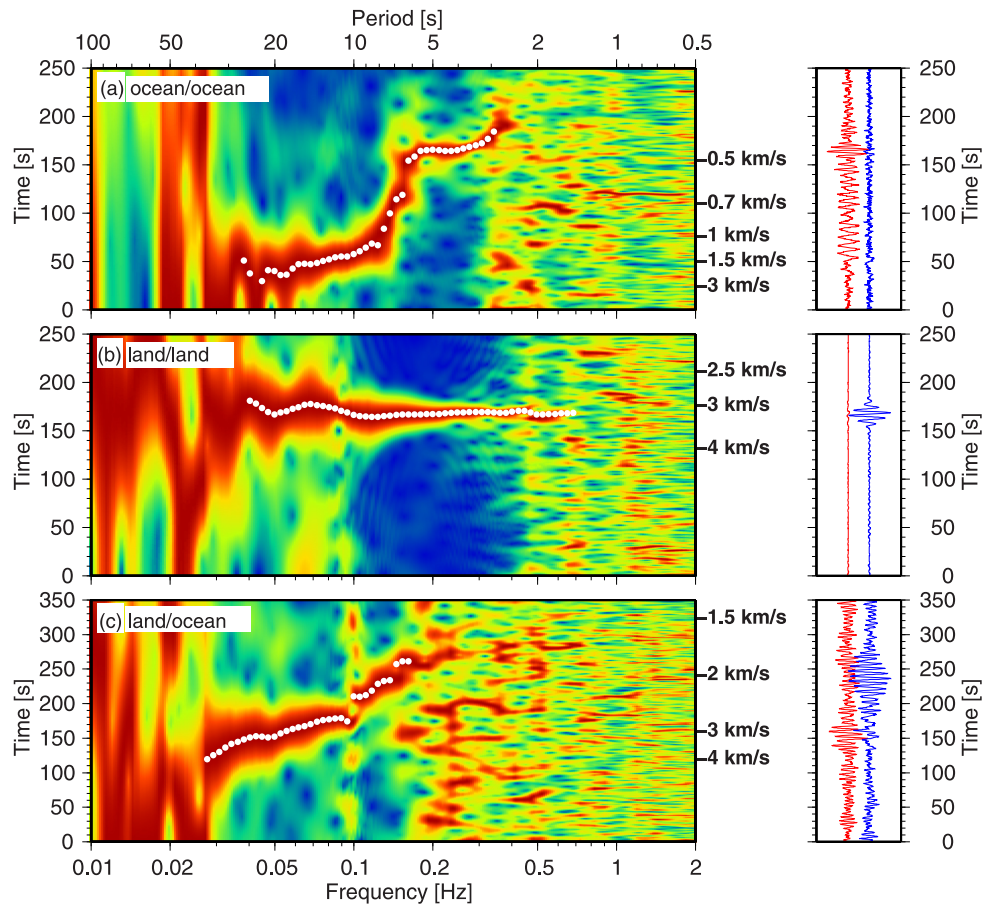
Figure 3. Examples of dispersion curve analysis: (a) Analysis of hydrophone component seismic records (right-hand panel) between OBS station WPO08 and WPO07 at the WR (locations indicated in Fig. 1). Note the strong asymmetry between the causal (red) and acausal (blue) phases in the right-hand panel. The dispersion curve analysis is in the left-hand panel (red colours indicate high, blue colours low amplitudes). Traces are normalized in every frequency/period band, traveltime picks are indicated by white dots. Corresponding group velocities are indicated at the right-hand side of the panel. A highly dispersed surface wave curve (Rayleigh/Scholte phases) can be identified for signal periods between 3 and 30 s. (b) Analysis of vertical component of a land station pair between WP01 and WP15 (locations indicated in Fig. 1). For this data example, the surface wave phase is only slightly dispersive and can be identified for signal periods between 2 and 30 s. (c) Analysis of a station pair between ocean station WPO07 (hydrophone component) and land station WP15 (vertical component; locations indicated in Fig. 1). The surface wave train can be identified for signal periods between 6 and 35 s. The dispersion curve has an intermediate character compared to those of purely oceanic and land wave propagation paths.

3 INVERSION

To infer the 3-D distribution of Vs we applied a two-step inversion: firstly, we used the traveltime picks (dispersion curves) to invert for the 2-D distribution of group velocity at every frequency, followed by a local depth inversion at every grid cell. At every signal period between 1 and 40 s (75 individual periods, spaced logarithmically), these traveltime picks (or Rayleigh wave group velocities) were used to derive a 2-D group velocity map applying the FMST (fast marching surface tomography) package (Rawlinson & Sambridge 2005). The inversion grid was composed of 40 by 30 square cells with a size of ∼25 km. Picking outliers (typically 5–10 per cent) were automatically removed during the inversion according to the technique of Ryberg *et al.* (2016b).

The complete set of 75 group velocity maps was treated as a set of virtual dispersion curves at every inversion cell. These virtual dispersion curves contain information from both, the local Earth structure and the local water depth.

In the second inversion step we performed a search for a local 1-D Vs model by inverting the previously derived virtual dispersion curve. By considering that ambient noise recorded at the ocean floor is composed of Scholte waves, we assume a local (grid cell specific) water depth (zero onshore) as a first (fixed) layer in the model, thus decomposing the influence of the water column from the crustal and upper mantle velocity structure. The inversion of surface wave dispersion curves for Vs structure is a non-unique and non-linear problem. In this work we apply a Bayesian formulation that represents the solution of the inverse problem in terms of the posterior probability density (PPD) of the geophysical model parameters, that is S-wave velocity structure. We use a McMC method with an implementation of Metropolis–Hastings sampling to provide an unbiased sample from the PPD to finally compute velocity averages and their uncertainties. A transdimensional and hierarchical version of the McMC method (Bodin *et al.* 2012, dispersion curves only) provides additional estimates of data error statistics (data noise) and appropriate model parametrization (i.e. number of layers). By using wide priors, including physically quite unrealistic velocities,
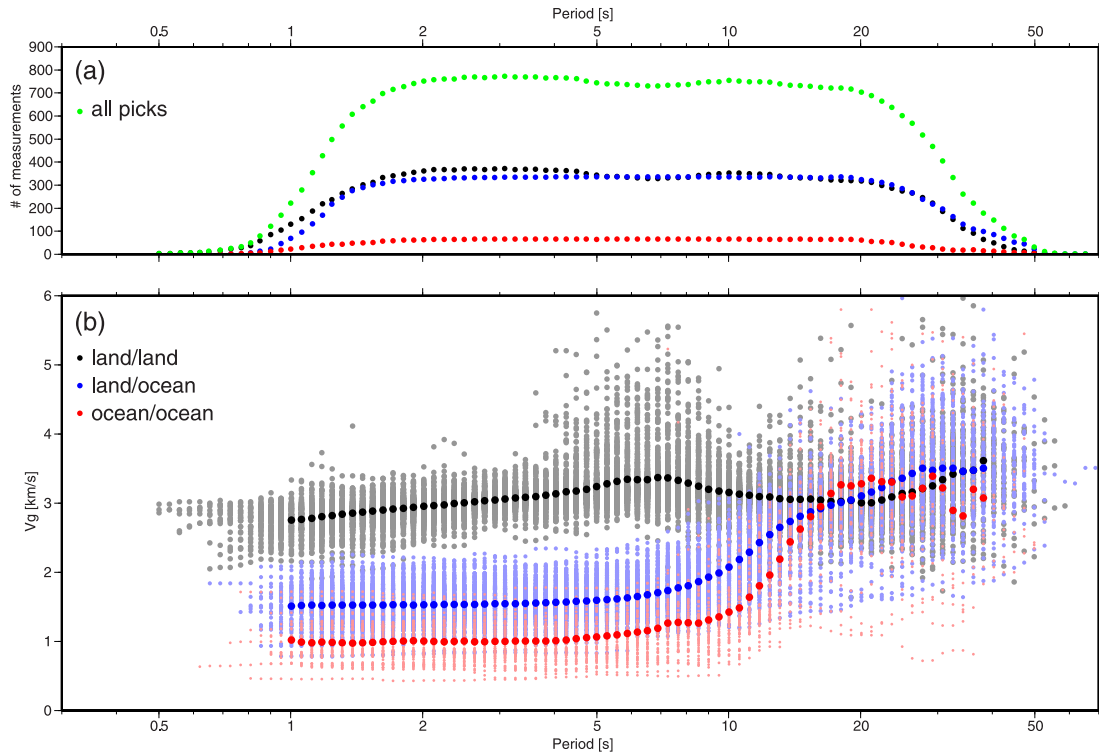
Figure 4. (a) Number of measurements as a function of signal period. Black, blue and red dots denote the land–land, land–ocean and ocean–ocean paths, respectively, Green dots represent the sum of all data. (b) Rayleigh wave group velocity measurements. Light grey, light blue and light red dots represent individual group velocity determinations, black/blue/red dots show the average dispersion curve. Lines and dots in black lines show the average group velocities for land paths, blue indicate ocean–land paths and red colours stand for purely oceanic paths. For the OBS data, hydrophone and vertical component cross correlations virtually coincide.

we can derive a large ensemble of velocity models fitting the observations from which the inference of the PPD can be made. This choice results in PPDs (velocity models) which almost exclusively depends on the data alone (and not based on any *a priori* assumptions).

We tested the inversion with synthetic data sets for known velocity models, assuming Vp/Vs ratios and density values according to Brocher (2005). We calculated for a given model the dispersion curve, added Gaussian distributed noise (velocity errors with RMS of 0.05 and 0.10 km s^{-1} for onshore/land and offshore/ocean-bottom locations, comparable to the remaining misfits of real data) and inverted them. To further accelerate the inversion, we implemented the algorithm on 1000 CPUs, sampling the model space simultaneously and independently. The first 10 000 models of every chain were discarded as burn-in steps, only after which the model sampling algorithm was assumed to have been converged. From the following 5000 models, every 200th model visited was selected for the ensemble inference. When surface wave dispersion data are inverted alone, average velocities are well recovered for a continental inversion cell, see Fig. 5, but, as expected, discontinuities are only poorly constrained, especially at larger depth. The velocity uncertainty (grey band) is increased at those discontinuities. However, the likelihood of a velocity discontinuity (transition probability) at a given depth has a maximum in the expected depth ranges, where the recovered Moho appears at the correct depth of 30 km with an apparent velocity of 3.9 km s^{-1}. In the presence of a water layer, the capacity to recover discontinuities is even further degraded, that is the models get significantly smoothed with increasing depth, however average velocities could be well reconstructed (Fig. 6).

Applied to the real data, we could invert for velocity models at 573 locations (centred grid cells), covered by the traveltime tomography. Most onshore cell models show a velocity discontinuity around 30 km depth, which we interpret as the Moho (typical example is shown in Fig. 7). Offshore cells show a sharp velocity increase in a depth range between 10 and 20 km, an example of which is shown in Fig. 8. This jump can be already inferred from the shape of the group velocity. Compared to the results of the recovery of synthetic models offshore (Fig. 6), this discontinuity could be interpreted as the Moho, thus, hindering the determination of the crustal thickness.

From these local 1-D models a final 3-D model was constructed by horizontal interpolation. To assess the horizontal resolving power of our imaging technique we performed checkerboard tests to evaluate the spatial resolution (see Fig. 9), where we found good horizontal resolution in the onshore part and, given the experiment geometry, reduced resolution mostly offshore.

Given the sensitivity distribution of Rayleigh waves with depth (depth dependent smoothing), sharp discontinuities (i.e. Moho) are, if recovered at all, not well constrained. Thus, reliable absolute crustal thicknesses, especially offshore, are relatively poorly constrained when analysing fundamental mode Rayleigh wave dispersion alone. This might potentially hinder a direct comparison with seismic wide-angle and refraction velocity models. Nevertheless, qualitative conclusions, that is regions with thin or thick crust, fast or slow crustal velocities, can be revealed from the 3-D model and are discussed jointly with existing active source seismic data along 2-D profiles.
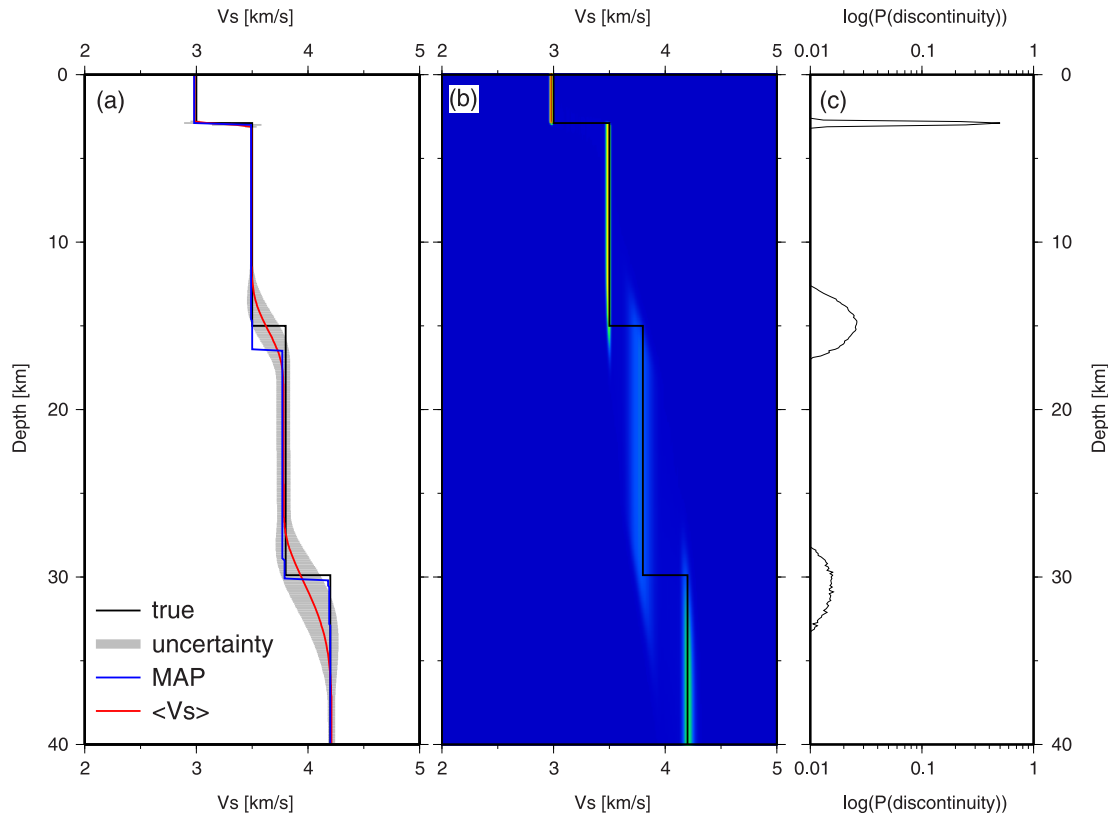
Figure 5. Results of the synthetic test: recovered *Vs* distribution for a model without a water layer. The left-hand panel (a) shows the results for *Vs* inversion for the synthetic model (black line). The red line shows the posterior mean model (average solution) constructed by taking the average *Vs* at each depth across the ensemble solution. The grey region shows the *Vs* standard deviation (one σ uncertainty). The blue line follows the maximum of the distribution of *Vs* with depth, representing the maximum *a posteriori* probability (MAP) estimate. The middle panel (b) shows a histogram plot of *Vs* versus depth (warm colours correspond to high probabilities) for all models beyond the burn-in phase. The right-hand panel (C) shows the probability of the occurrence of a velocity discontinuity at a given depth. The average velocity (red line, left-hand panel) fits well the input model, with increased uncertainty around velocity discontinuities. As expected, the sharpness of the recovered discontinuities quickly degrades with depth. At the depth of the Moho the velocity is around 4 km s^{-1}.

4 RESULTS

The final 3-D *S*-wave model is presented by a subset of horizontal slices and vertical sections. The model was sliced horizontally at six depths from 4 to 35 km (Fig. 10). Generally, all depth slices show a clear separation between the continental and oceanic crust and upper mantle. Offshore, the shallowest parts ($\leq$8 km) of the crust is characterized by a strongly decreased (with respect to other parts of the model) *S*-wave velocity at the WR and in the adjacent ocean basins relative to onshore and north of the ridge regions (Fig. 10, marker C). While onshore *S*-wave velocities appear to be quite homogeneous (Fig. 10, marker A), the offshore velocity pattern is more complex: that is regions north and south of the WR far away from the coast are heterogeneous, and the region north of the WR (Namibe Basin) is characterized by high *Vs* (again, with respect to other regions in the study area, Fig. 10, marker B). The depth slice at 12 km depth shows a pronounced velocity decrease beneath the WR (Fig. 10, marker D), indicating a thicker crust, which is in good agreement with Fromm *et al.* (2015, 2017) and Heit *et al.* (2015). Generally, at depths greater than 15 km, the velocities are higher offshore than below the continent, indicating that high-velocity lower crust and/or upper mantle structure is imaged offshore (Fig. 10, marker C). This observation agrees with the observation of magmatically underplated, high-velocity, lower crust of Fromm *et al.* (2015, 2017).

To better visualize the complexity of the rifted margin we present the results in different vertical sections (Fig. 11), both parallel and perpendicular to the coast. Because the depth inversion was carried out for every cell individually, some artefacts (vertical columns) caused by the variable number of signal frequencies are involved in the local depth inversion. The onshore mid- and lower-crustal *S*-wave velocities show little lateral variability around 3.5 km s^{-1} in the upper crust, and 4 km s^{-1} in the lower crust/upper mantle as expected from the flat dispersion curve, respectively (Fig. 11, marker A). Values above 4.1 km s^{-1}, typically at depths >30 km, are interpreted as mantle material, yet the depth resolution is already significantly degraded due to the sensitivity of the surface waves. All sections across the continent–ocean transition (A–A', B–B', C–C') show a thin layer of very low *S*-wave velocities (<2 km s^{-1}, red colour, sediment layer, marker C in Fig. 11) of several kilometres thickness extending from 100 to 250 km offshore. In the Namibe Basin slice (C–C') the low velocity layer extends only 100 km offshore, but extends further offshore along WR (B–B') and in the Walvis Basin (A–A'). The underlain middle crust (at <12 km depth, marker D in Fig. 11) offshore shows velocities between 2.5 and 3 km s^{-1}, which is lower than those of the continental counterpart. This middle crust thins out rapidly in the Namibe Basin ~150 km away from the coast (Fig. 11 slice C–C'), extends along the entire WR (Fig. 11 slice
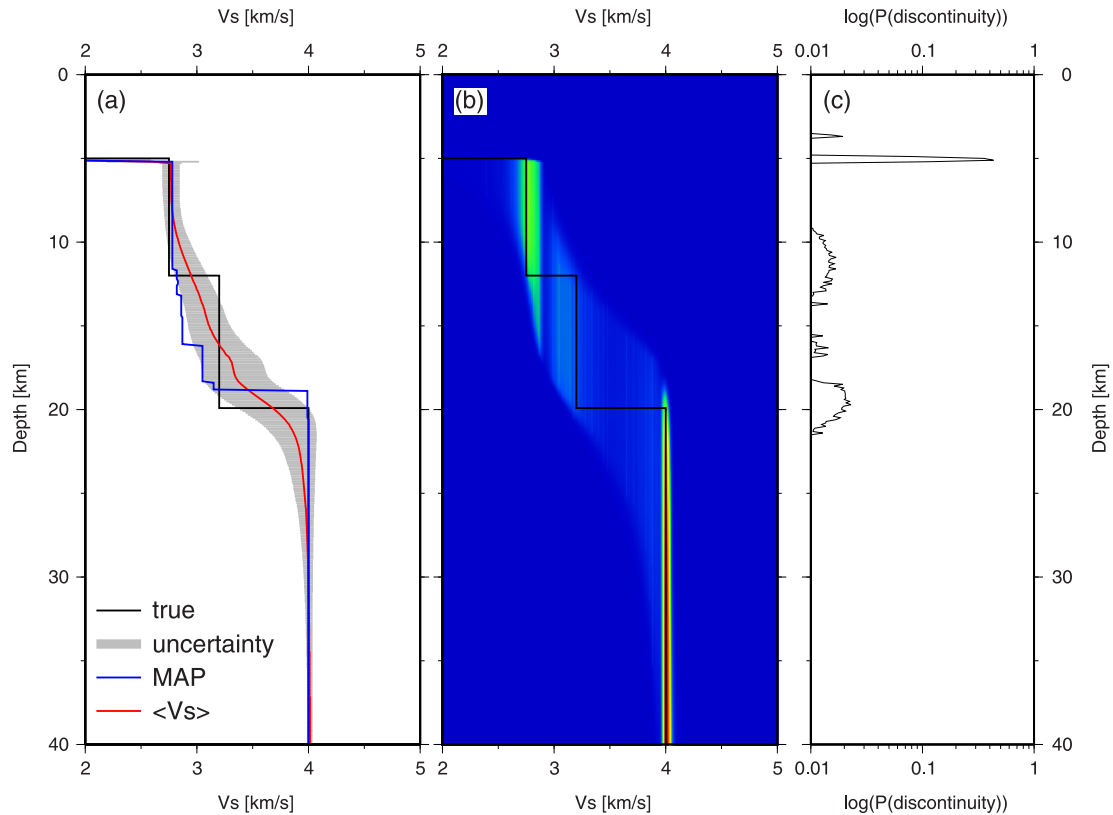
Figure 6. Similar to Fig. 5, but now with a water layer of 5 km above the model. In this case the resolving power for discontinuities is even further decreased, however, the average model (red line) could be reasonably well recovered. At the true Moho depth the recovered velocity does not show a sharp increase but a gradient transition zone centred at $\sim$3.7 km s^{-1}, while the probability of the occurrence of a velocity discontinuity (c) shows a clear peak at the correct depth.

B–B'), and could be observed up to $\sim$350 km offshore in the Walvis Basin (Fig. 11 A–A'). At the landfall of the WR we observe a slight velocity increase in the middle crust (Fig. 11, slices F–F', A–A' and B–B', marker B in Fig. 11), which does not appear to extend much further inland.

While the onshore coast-parallel section is quite featureless, except the slight velocity increase, (Fig. 11 slice F–F', marker B), both sections across the WR show typical crustal velocities reaching down to $\sim$15 km depth (Fig. 11 slices E–E', D–D', marker D), extending further south into the Walvis Basin (Fig. 11 slice E–E'), while being absent in the Namibe Basin. The crustal velocities ($>$10 km) are distributed symmetrically across the WR far offshore (Fig. 11 slice D–D', marker D) and show a strong asymmetry closer to the coast (Fig. 11 slice E–E', marker D). The shallow low velocities (down to a few km below the seabed) could only be imaged along profile E–E' and are probably too thin to be imaged in the deeper parts of the Namibe and Walvis Basins. The smallest signal periods of the recovered dispersion curves ($>$1 s) limit a reasonable well imaging of the shallow, thin and slow sedimentary layers.

5 DISCUSSION

The junction of the WR with the Namibian coast was subject of extensive passive seismic investigations in 2010/2011 to document the distribution of hotspot volcanism of the Tristan plume. While onshore conjugate continental flood basalts (CFB) in South America (Parana CFB) and northern Namibia (Etendeka CFB) are well documented (i.e. Miller 2008), the amount of erupted offshore hotspot material was only poorly known. In total six 2-D deep seismic sounding lines (Fig. 12) were acquired on- and offshore (Bauer *et al.* 2000; Fromm *et al.* 2015, 2017; Ryberg *et al.* 2015; Planert *et al.* 2017). Passive seismological studies (Heit *et al.* 2015) determined the seaward extension of a Large Igneous Province (LIP), the crustal structure of the WR and how the hotspot volcanism modified the lower continental crust in the area. One of the surprising results is that the continental crust in NW Namibia was only modified at the junction with the WR close to its present-day coastline for approximately 100×100 km^2 by the massive CFB eruptions prior or synchroneously to the opening of the South Atlantic (Bauer *et al.* 2000; Fromm *et al.* 2015, 2017; Ryberg *et al.* 2015; Planert *et al.* 2017). The WR itself is interpreted as the hotspot track of the Tristan plume, which continuously formed during the opening of the South Atlantic. The shape (morphology) of the hotspot track strongly varies from the Namibian coast towards the present-day hotspot position close to Tristan da Cunha Island. The initial volcanism formed a massive ridge, with up to 35-km-thick igneous crust, while the present-day active hotspot region around the Tristan Island is characterized by scattered seamounts (O'Connor & Duncan 1990; Milner *et al.* 1995; Ewart *et al.* 2004; O'Connor & Jokat 2015; Jokat & Reents 2017; Schlömer *et al.* 2017).
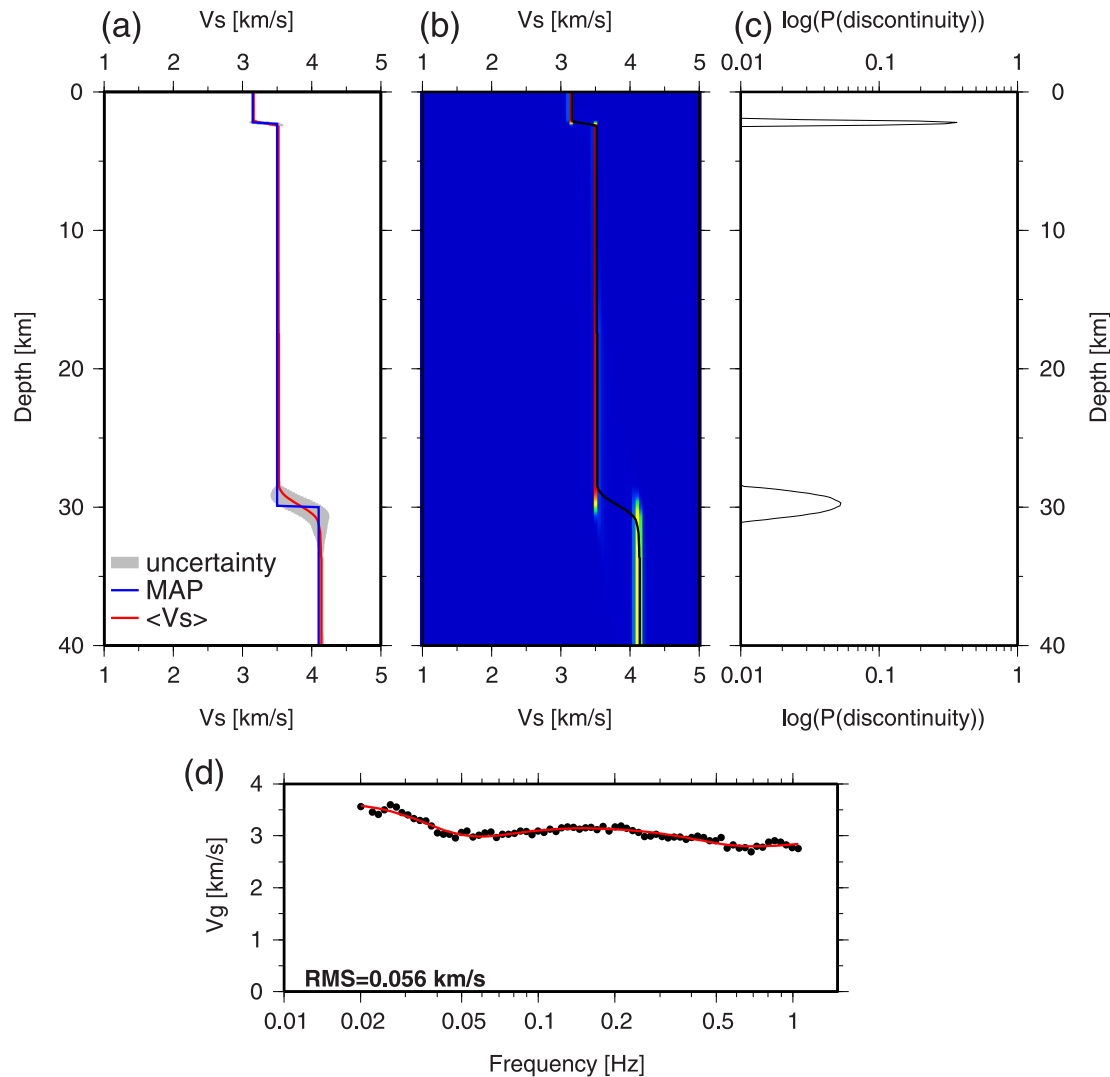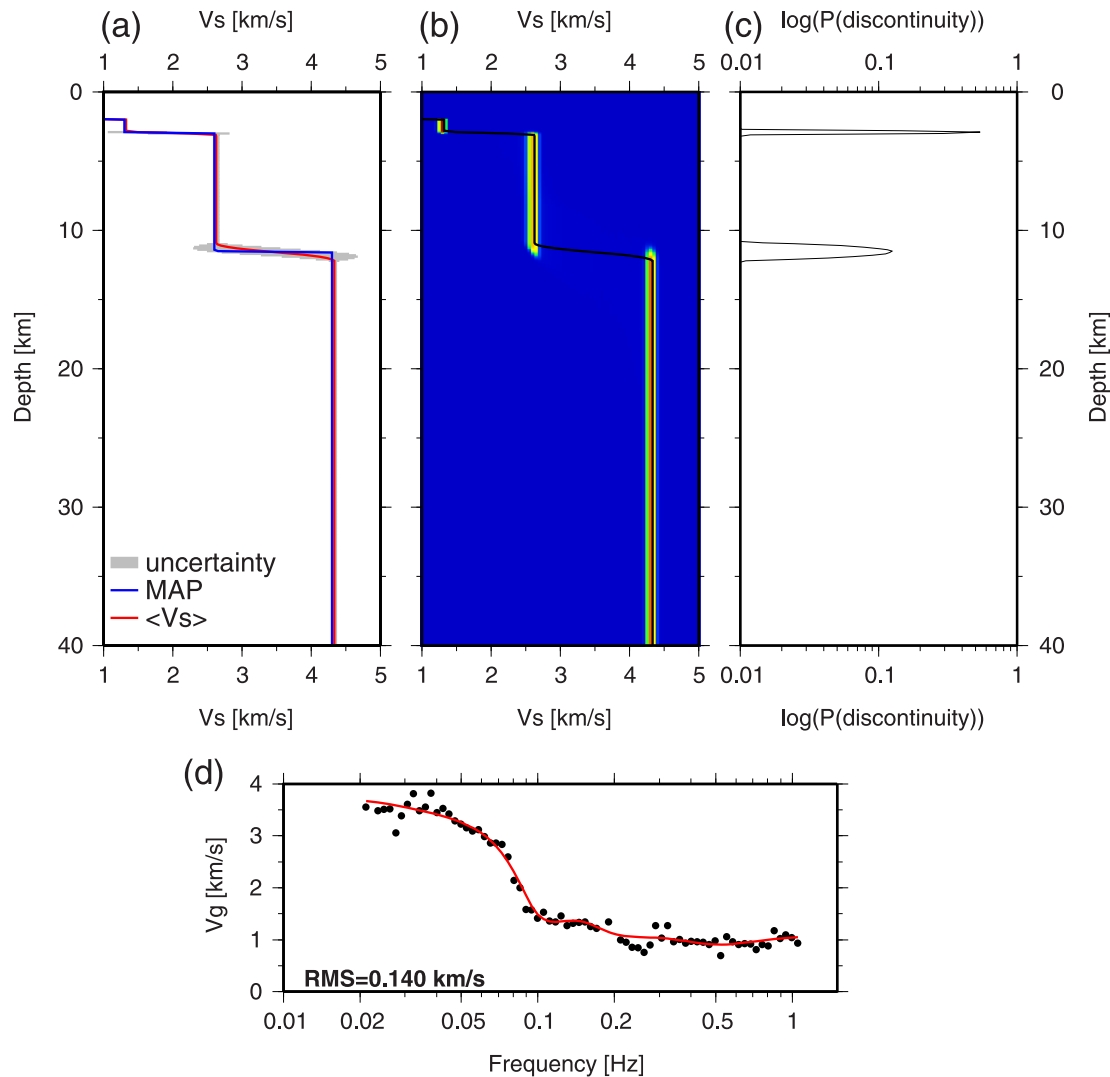
Figure 7. Similar to Fig. 5, but this time for the real data inversion of an onshore cell (yellow marked onshore cell in Fig. 1). The model shows two clear velocity discontinuities at 2 and 30 km depth. The latter one we interpret as the Moho. The bottom diagram (d) shows the data fit (data: black dots, average model: red line).

While the deep seismic sounding (seismic wide-angle and refraction) data provide a detailed insight into the general offshore crustal structure along some 2-D sections, it remained an open question if and how the crustal structure varies in 3-D (Fig. 12). Here, we use records of seismological onshore and offshore stations to provide a 3-D view of the crustal fabric at the junction of the WR with the Namibian coast. Although, the ANT method does not provide the same details of the crustal structures as deep seismic sounding data, it is a valuable tool to interpolate and extrapolate their results. From the rock ages of the two CFB provinces, the first eruptions related to the Tristan plume are well documented to happen around 132 Ma, a time when the South Atlantic started to open in our research area. Previous investigations had shown that the Tristan plume did not largely or massively modify the Namibian continental margin (Ryberg *et al.* 2015; Fromm *et al.* 2017; Planert *et al.* 2017) as suggested before because of the presence of the onshore Etendeka CFB with an assumed plume head diameter of 1000–2000 km. A High Velocity Lower Crustal Body (HVLCB) below WR with *P*-wave velocities well above 7.0 km s^{-1} has been interpreted to represent added plume-related magmatic material. At the junction of the WR with the coast, the HVLCB has a N–S extent of approximately 100 km (Ryberg *et al.* 2015) and reaches only 100 km eastward into the continental crust (Fromm *et al.* 2015; Heit *et al.* 2015).

We interpret the shallow, very low velocities recovered offshore as being caused by a sedimentary cover (red colour in Fig. 11) of variable thickness. Sedimentary structures are not in the focus of our study, but much better constrained by seismic refraction studies (Fromm *et al.* 2017; Planert *et al.* 2017). Slightly elevated *S*-wave velocities in the depth range down to 12 km compared to the area north of the WR (green colours marked D in Fig. 11), are interpreted as magmatically extruded and intruded material (Seaward Dipping Reflectors, SDRs), which formed during the initial phase of breakup and the evolution of the WR hotspot track. With a thickness of up to 10 km it corresponds to the upper/middle crust imaged by seismic refraction studies showing elevated *Vp* (above 7 km s^{-1}, Fromm *et al.* 2015, 2017; Planert *et al.* 2017). Therefore, the crust is classified as rifted continental/transitional upper crust close to the coast and thickened oceanic crust further offshore

Figure 8. Same to Fig. 7, but this time for the inversion of an offshore cell (yellow marked offshore cell in Fig. 1). The model shows two clear velocity discontinuities a few km below sea bed and around 12 km depth. It is unclear if the latter one represents the Moho. The bottom diagram (d) shows the data fit (data: black dots, average model: red line).

along the WR with a strong variability across the WR. Information on lower crustal velocities and Moho depths are not imaged with the offshore set-up.

From the onshore cross sections in Fig. 11, there are no indications that the initial WR magmatism has significantly modified large parts the continent (slice F–F' in Fig. 11). Weak indications for a slight upper and mid-crustal velocity increase (shallow blue colours, marker B) at the landfall region of WR are found, which extend ∼100 and ∼200 km north and south of the ridge axis, respectively. This velocity increase, although not very strong, might be associated with the lower crustal high-velocity body ($Vp > 7$ km s^{-1}; ∼20 km thick at maximum) observed by Ryberg *et al.* (2015). Using the receiver function method, Heit *et al.* (2015) also found thick crust and high Vp/Vs ratio at the landfall of the WR. These high Vp/Vs ratios, together with the high Vp anomaly of Ryberg *et al.* (2015) could be consistent with high Vs values obtained here by our analysis and were interpreted as the effects of magmatic underplating induced by a localized mantle thermal anomaly in form of a plume. Yuan *et al.* (2017) observed early arrivals of the mantle-transition discontinuity phases and also suggest high seismic velocities in the upper mantle and at the base of the crust beneath the WR.

Looking at the depth slice at 12 km (Fig. 10, marker E), relatively low Vs far offshore in the Walvis Basin indicate the presence of oceanic crust, not affected by magmatic processes associated with the massive break up/hot spot volcanism. Therefore, the boundary towards higher velocities at this depth (Fig. 10; blue colours south of WR) is interpreted with some uncertainty (choice of colour scale) as the landward limit of normal (or true or Penrose type) oceanic crust.

We interpret the high *S*-wave velocities, imaged in the lower crust in the Walvis Basin (Fig. 10, at depth 12 km) south of the WR (blue colours) but closer to the Namibian coast as magmatic material emplaced during the continental breakup. Seismic refraction lines further south along the continental margin unravelled a massive high velocity lower crustal body (Bauer *et al.* 2000) and is likely associated with the formation of SDRs along the South African continental margin (Franke 2013; Koopmann *et al.* 2014a). In the study area these high velocities
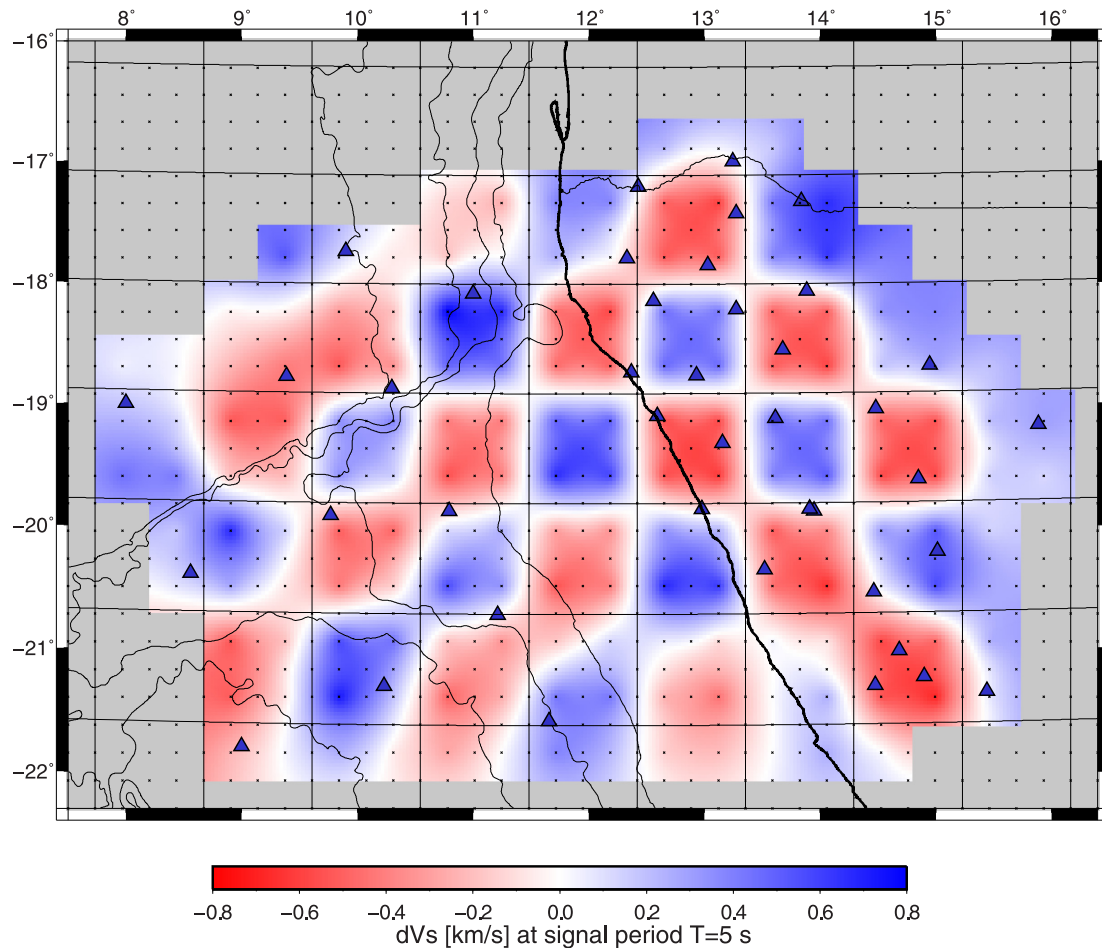
Figure 9. Results of checkerboard recovery test (relative velocity scale) at signal period $T = 5$ s (~5 km depth). For a synthetic model with checkerboard shaped velocity anomalies, traveltimes were calculated, noise was added (time jitter, Gaussian distributed with standard deviation of 2 s, similar to the RMS misfit of the 2-D inversion at that period), and 2-D group velocity maps were inverted, similar to the real data processing. The checkerboard patterns (square boxes) are recovered with sufficiently high resolution in the onshore part of the study region and with some degradation offshore. Small dots indicate the inversion cells. The horizontal resolving power is mostly controlled by the first inversion set-up (traveltime tomography).

coincide well with the SDRs distribution (Fig. 12). The region of elevated lower crustal *S*-wave velocities agrees well with the regions of increased crustal thickness derived from controlled source, amphibious P_n-tomography (Ryberg *et al.* 2016a) and onshore receiver functions (Heit *et al.* 2015 and Yuan *et al.* 2017).

When analysing surface wave data alone, it is difficult to delineate the Moho (sharp velocity boundary) and therefore estimate the absolute crustal thickness. As mentioned before, the applied method does not permit to derive reliable absolute values of crustal thickness, given the limitation of the method with respect to sharp discontinuities. Therefore, we decided to show the 3.9 km s^{-1} velocity isoline, which can be used as a relative proxy to the crustal thickness, being aware of its limitation to indicate absolute Moho depth (see recovery of synthetic dispersion curves in Figs 5 and 6). However, this is not valid for the WR. Interpreting this isoline as the Moho boundary, we would interpret the crust–mantle boundary beneath the WR at less than ~15 km depth (Fig. 11, slice B–B'). However, the difference to more reliable Moho depth calculations from the seismic refraction studies (~31 km; Fromm *et al.* 2015, 2017) is too large. A typical feature in their seismic refraction velocity–depth model is a HVLCB at 15–18 km depth (Fromm *et al.* 2015, 2017). Consequently, we suggest that we have imaged the top of this HVLCB marking a depth range where faster material is present. Probably because of poor resolution, the isoline does not represent the Moho in the deepest waters of Walvis Basin/WR and the Namibe Basin. We interpret that the 3.9 km s^{-1} isoline is a good estimation for Moho depth on land, judging from the aspect of typical dispersion curves in cells located on land (Fig. 7) and their respective recovery test (Fig. 5). Even if the absolute estimates of the crustal thickness might be uncertain, the spatial distribution of relative thickness differences is well imaged by the ambient noise tomography. The recovered onshore crustal thickness of ~35 km is consistent with the values derived by the receiver function method (Heit *et al.* 2015).

Below the WR and the Walvis Basin, but not below the continent, there is some indication of slightly elevated upper mantle *S*-wave velocities (magenta colours in Fig. 11, marker E). This velocity increase, although not well constrained at depth, appears below ~15 km below the thickened offshore crust.
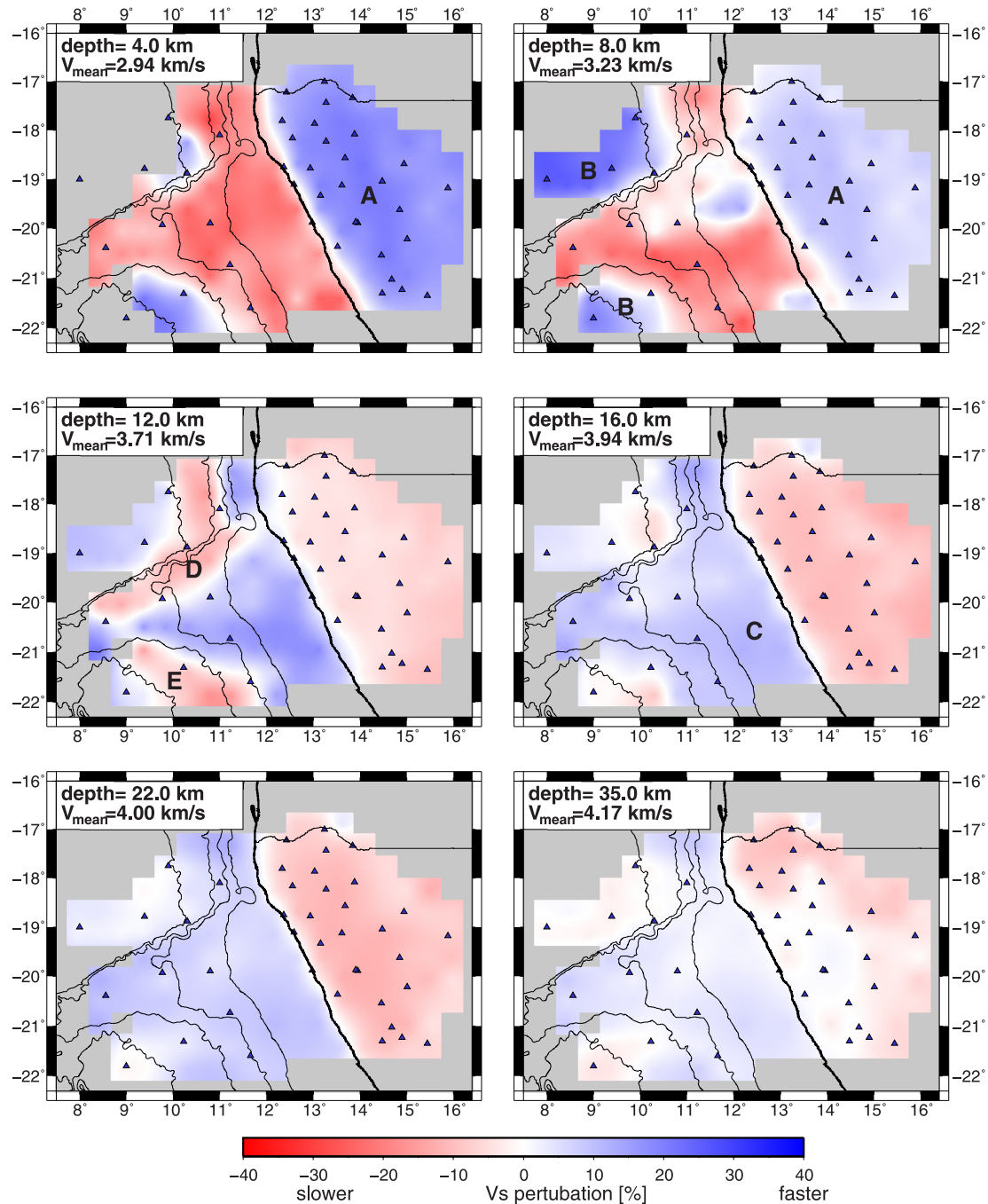
Figure 10. Horizontal depth slices (relative scale) through final 3-D *Vs* model. Triangles show the seismic network. Depths (below sea level) and average velocities are indicated, grey areas are not inverted or have poor resolution. Features A–E are discussed in the text.

The observed characteristic asymmetry in crustal properties across the WR was already imaged by amphibious refraction seismic data in the study area along three profiles (Fromm *et al.* 2015, 2017; Planert *et al.* 2017). As mentioned above, although no absolute values for crustal thickness and velocities at greater depths can be derived reliably by our tomographic technique, our model qualitatively coincides well with previous studies along these seismic profiles.

6 CONCLUSIONS

We have shown that we can successfully derive a 3-D *S*-wave velocity model from an amphibious seismic ambient noise data set using a combination of tomographic traveltime inversion followed by a Bayesian McMC based depth inversion. Fig. 12 shows an overview of our findings, combined with summarized models from controlled source seismic investigations in the study region (Koopmann *et al.* 2014b; Fromm *et al.* 2015, 2017; Ryberg *et al.* 2015; Planert *et al.* 2017) and surroundings (Bauer *et al.* 2000), the regional gravity field (free-air)
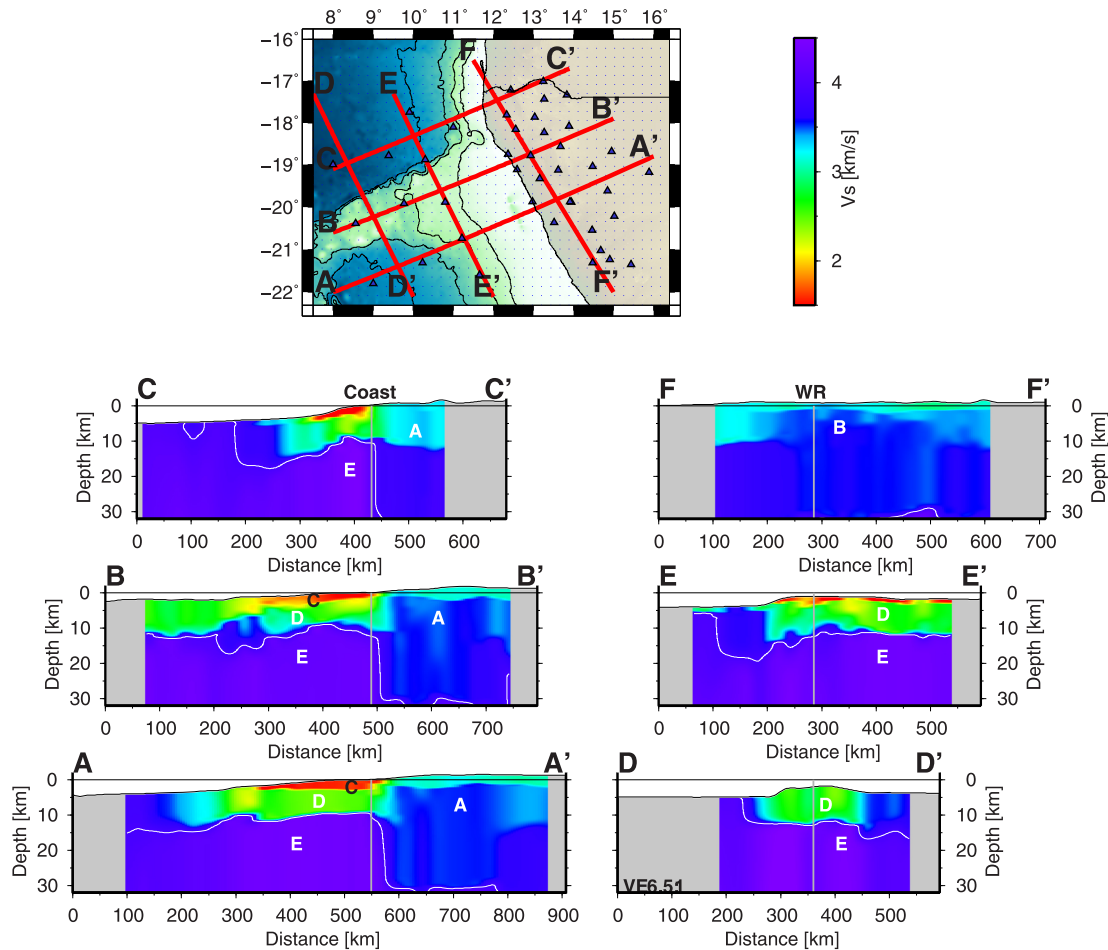
Figure 11. Vertical cross sections (absolute velocity scale) through final *Vs* model across the continental margin, coast-parallel slice (right-hand panel) and coast-perpendicular slice (left-hand panel) aligned at the shore line (left-hand panel) or WR (right-hand panel). Slice A–A' crosses the Walvis Basin into the continent. It shows a wide (∼300 km), ocean–continent transition with relatively thick crust. Slice B–B' along the WR shows a thickened crust compared to the crust in the Namibe Basin. Slice C–C' crosses the Namibe Basin. It shows a typical oceanic thin crust (as seen by controlled source seismic data in the region, Fromm *et al.* 2015, 2017). The onshore part of all cross sections shows a fast and thick continental crust. Slice D–D' crosses the WR ∼400 km offshore. It shows a very localized (<150 km wide) thickened crust at WR and thicker crust towards South (Walvis Basin) in comparison to the Namibe Basin. Slice E–E' crosses the WR from the Namibe Basin (thin crust) and continues into the Walvis Basin with a thickened crust. Slice FF' samples the continental crust onshore. Location of the slices are marked on the map. Grey lines indicate the position of the shore line or the centre of WR (identical to line B–B'). The $Vs = 3.9 \, km \, s^{-1}$ isoline in white is shown as a relative proxy to the crust–mantle transition, see discussion in the text. The aspect ratio is 6.5:1. Some artefacts (vertical bars/columns) are present caused by the depth inversion since no post-inversion horizontal smoothing was applied. Features A–E (white symbols) are discussed in the text.

and the distribution of SDRs as background information. The 3-D velocity model, obtained by our ambient noise investigations, fits with the seismic velocity anomalies recovered along several seismic lines (high velocity bodies in the lower crust, overall thickened crust) of previous studies, filling the gap in-between the lines.

The results obtained by our ambient seismic noise tomographic method show that the oceanic crust has different seismic velocities to the north and south of the WR, covering mostly the regions where SDRs were previously detected. The Walvis Basin is located in an area of thickened oceanic crust south of the WR. The abrupt change in velocities at the landfall of the WR has already been observed by other studies. These results are confirmed with a different method. Furthermore, with the data presented here we are able to extend this anomaly to a larger area (3-D). The higher velocities (well above 4.1 km s^{-1}) observed in the upper mantle are rather local (Fig. 11, marker E) and cannot be observed in the entire region. This indicates that the thermal effects of the plume associated with the evolution of the WR are comparatively minor and can only be observed below the WR and at the base of the Walvis Basin oceanic crust. Finally, our study supports interpretations from 2-D seismic refraction profiles are also valid in a more regional sense.

ACKNOWLEDGMENTS
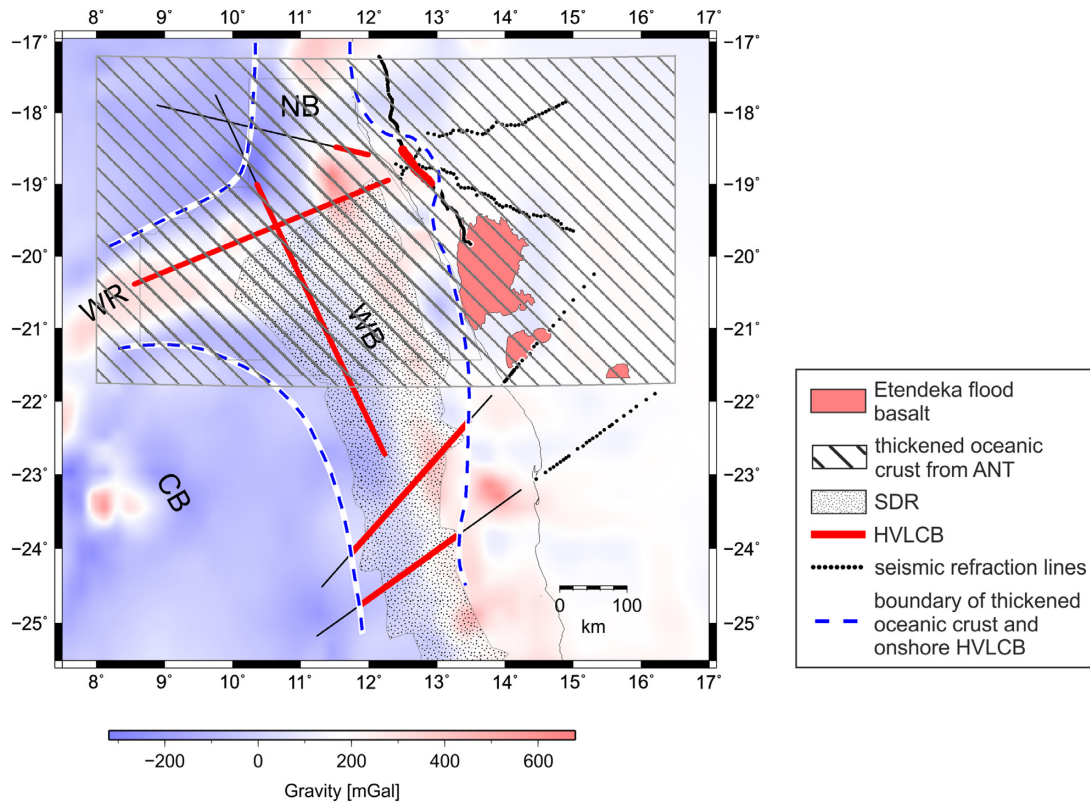
Figure 12. Gravity map (free-air anomaly) of the study region (box) and surroundings. (WR, Walvis Ridge; NB, Namibe Basin; WB, Walvis Basin; CB, Cape Basin). Black dots/lines indicate location of the wide-angle seismic line (Ryberg *et al.* 2015; Planert *et al.* 2017, Fromm *et al.* 2015, 2017; Bauer *et al.* 2000). Thick red zones along these lines mark the presence of high velocity mid- and lower crustal bodies, both on- and offshore. In the finely hashed region SDRs had been detected (Koopmann *et al.* 2014b). The sparsely hashed area in the box (ambient noise study region) summarizes the region of thickened and/or higher velocity lower crust, blue dashed lines indicate the boundary to more classical oceanic and continental crust based on the controlled source seismic studies. The hashed area corresponds to the region of elevated velocities in Fig. 10 (depth slice at 16 km). Pink areas show the Etendeka flood basalts (modified from Gladczenko *et al.* 1997).

DATA AVAILABILITY

Waveform data are archived at the GEOFON (Heit *et al.* 2010) and are freely accessible. The model is provided in the Supplement.

REFERENCES

Ball, J.S., Sheehan, A.F., Stachnik, J.C., Lin, F.-C., Yeck, W.L. & Collins, J.A. 2016. Lithospheric shear velocity structure of South Island, New Zealand, from amphibious Rayleigh wave tomography, *J. geophys. Res.,* **121,** 3686–3702.

Bauer, K. *et al.* 2000. Deep structure of the Namibia continental margin as derived from integrated geophysical studies, *J. geophys. Res.,* **105,** 25 829–25 853.

Bauer, K., Schulze, A. Ryberg, T. Sobolev, S.V. & Weber, M. 2003. Classification of lithology from seismic tomography, a case study from the Messum igneous complex, Namibia, *J. geophys. Res.,* **108**(B3), https://doi.org/10.1029/2001JB001073.

Bensen, G.D., Ritzwoller, M.H., Barmin, M.P., Levshin, A.L., Lin, F., Moschetti, M.P., Shapiro, N.M. & Yang, Y. 2007. Processing seismic ambient noise data to obtain reliable broadband surface wave dispersion measurements, *Geophys. J. Int.,* **169,** 1239–1260.

Bodin, T., Sambridge, M., Tkalčić, H., Arroucau, P., Gallagher, K. & Rawlinson, N. 2012. Transdimensional inversion of receiver functions and surface wave dispersion, *J. geophys. Res.,* **117,** B02301, doi:10.1029/2011JB008560.

Brocher, T.M. 2005. Empirical relations between elastic wavespeeds and density in the Earth's crust, *Bull. seism. Soc. Am.,* **95,** 2081–2092.

Campillo, M. & Paul, A. 2003. Long-range correlations in the diffuse seismic coda, *Science,* **299,** 547–549.

Campillo, M. & Roux, P. 2014. Seismic imaging and monitoring with ambient noise correlations, in *Treatise on Geophysics,* eds 2nd edn, Vol. **1,** pp. 256–271, eds Romanowicz, B. & Dziewonski, A., Elsevier.

Colli, L., Fichtner, A. & Bunge, H.-P. 2013. Full waveform tomography of the upper mantle in the South Atlantic region: imaging a westward fluxing shallow asthenosphere?, *Tectonophysics,* **604,** 26–40.

Corela, C., Silveira, G., Matias, L., Schimmel, M. & Geissler, W.H. 2017. Ambient seismic noise tomography of SW Iberia integrating seafloor- and land-based data, *Tectonophysics,* **700-701,** 131–149.

Dziewonski, A., Bloch, S. & Landisman, M. 1969. A technique for the analysis of transient seismic signals, *Bull. seism. Soc. Am,* **59,** 427–444.

Ewart, A., Marsh, J.S., Milner, S.C., Duncan, A.R., Kamber, B.S. & Armstrong, R.A. 2004. Petrology and geochemistry of Early Cretaceous bimodal continental flood volcanism of the NW Etendeka, Namibia. Part 1: introduction, mafic lavas and re-evaluation of mantle source components, *J. Petrol.,* **45,** 59–105.

Feng, L. 2021. Amphibious shear wave structure beneath the alaska-aleutian subduction zone from ambient noise tomography, *Geochem. Geophys. Geosyst.,* **22,** doi:10.1029/2020GC009438.

Franke, D. 2013. Rifting, lithosphere breakup and volcanism comparison of magma-poor and volcanic rifted margins, *Mar. Petrol. Geol.,* **43,** 63–87.

Fromm, T., Planert, L., Jokat, W., Ryberg, T., Behrmann, J.H., Weber, M. & Haberland, C. 2015. South Atlantic opening: a plume-induced breakup? *Geology,* **43,** 931–934.

Fromm, T.L., Jokat, W., Ryberg, T., Behrmann, J.H., Haberland, Ch. & Weber, M., 2017. The onset of Walvis Ridge: plume influence at the continental margin, *Tectonophysics,* **716,** 90–107.

Gao, H. & Shen, Y., 2015. A preliminary full-wave Ambient-Noise Tomography Model Spanning from the Juan de Fuca and Gorda Spreading Centers to the Cascadia Volcanic Arc, *Seismol. Res. Lett.,* **86,** 1253–1260.

Gladczenko, T.P., Hinz, K., Eldholm, O., Meyer, H., Neben, S. & Skogseid, J., 1997. South Atlantic volcanic margins, *J. geol. Soc. Lond.,* **154,** 465–470.

Guerin, G., Rivet, D., Deschamps, A., Larroque, C., Mordret, A., Dessa, J. & Martin, X., 2020. High resolution ambient noise tomography of the Southwestern Alps and the Ligurian margin, *Geophys. J. Int.,* **220,** 806–820.

Hable, S., Sigloch, K., Stutzmann, E., Kiselev, S. & Barruol, G. 2019. Tomography of crust and lithosphere in the western Indian Ocean from noise cross-correlations of land and ocean bottom seismometers. *Geophys. J. Int.,* **219,** 924–944.

Harmon, N., Forsyth, D. & Webb, S. 2007. Using ambient seismic noise to determine short-period phase velocities and shallow shear velocities in young oceanic lithosphere, *Bull. seism. Soc. Am.,* **97,** 2009–2023.

Heine, C., Zoethout, J. & Müller, R.D. 2013. Kinematics of the South Atlantic rift, *Solid Earth,* **4,** 215–253, doi:10.5194/se-4-215-2013.

Heit, B., Yuan, X., Jokat, W., Weber, M. & Geissler, W. 2010. *WALPASS Network, Namibia, 2010/2012.* Deutsches GeoForschungsZentrum GFZ. doi:10.14470/1N134371.

Heit, B., Yuan, X., Weber, M., Geissler, W., Jokat, W., Lushetile, B. & Hoffmann, K. 2015. Crustal thickness and *Vp/Vs* ratio in NW Namibia from receiver functions: evidence for magmatic underplating due to mantle plume–crust interaction. *Geophys. Res. Lett.,* **42,** 3330–3337.

Jokat, W. & Reents, S. 2017.. Hotspot volcanism in the southern South Atlantic: geophysical constraints on the evolution of the southern Walvis Ridge and the Discovery Seamounts, *Tectonophysics,* **716,** 77–89.

Khoza, T.D., Jones, A.G., Muller, M.R., Evans, R.L., Miensopust, M.P. & Webb, S.J. 2013. Lithospheric structure of an Archean Craton and adjacent mobile belt revealed from 2-D and 3-D inversion of magnetotelluric data: example from southern Congo Craton in northern Namibia, *J. geophys. Res.,* **118,** 4378–4397.

Koopmann, H., Brune, S., Franke, D. & Breuer, S. 2014a. Linking rift propagation barriers to excess magmatism at volcanic rifted margins, *Geology,* **42,** 1071–1074.

Koopmann, H., Franke, D., Schreckenberger, B., Schulz, H., Hartwig, A., Stollhofen, H. & di Primio, R. 2014b. Segmentation and volcano-tectonic characteristics along the SW African continental margin, South Atlantic, as derived from multichannel seismic and potential field data, *Mar. Pet. Geol.,* **50,** 22–39.

Li, W., Yuan, X., Heit, B., Schmidt-Aursch, M.C., Almendros, J., Geissler, W.H. & Chen, Y. 2021. Back-arc extension of the central bransfield basin induced by ridge-trench collision: implications from ambient noise tomography and stress field inversion, *Geophys. Res. Lett.,* **48.** doi:10.1029/2021GL095032.

Longuet-Higgins, M. 1950. A theory of the origin of microseisms, *Phil. Trans. R. Soc. Lond., A,* **243,** 2–36.

Lynner, C. & Porritt, R.W., 2017. Crustal structure across the eastern North American margin from ambient noise tomography, *Geophys. Res. Lett.,* **44,** 6651–6657.

Miller, R.M. 2008.Early Cretaceous Etendeka Group, in *The Geology of Namibia,* Vol. **3,** pp. 17–11-17-57, ed. Miller, R. M., Geological Survey of Namibia.

Milner, S.C., Le Roex, A.P. & O'Connor, J.M. 1995.. Age of Mesozoic igneous rocks in northwestern Namibia, and their relationship to continental breakup, *J. Geol. Soc.,* **152,** 97–104.

Müller, R.D., Sdrolias, M., Gaina, C. & Roest, W.R. 2008. Age, spreading rates and spreading symmetry of the world's ocean crust, *Geochem. Geophys. Geosyst.,* **9,** Q04006, doi:10.1029/2007GC001743.

O'Connor, J. & Jokat, W., 2015. Tracking the Tristan-Gough mantle plume using discrete chains of intraplate volcanic centers buried in the Walvis Ridge, *Geology,* **43,** 715–718.

O'Connor, J.M. & Duncan, R.A. 1990. Evolution of the Walvis Ridge–Rio Grande Rise hot spot system: implications for African and South American plate motions over plumes, *J. geophys. Res.,* **95,** 17 475–17 502.

Planert, L., Behrmann, J., Jokat, W., Fromm, T., Ryberg, T., Weber, M. & Haberland, Ch. 2017. The wide-angle seismic image of a complex rifted margin, offshore North Namibia: implications for the tectonics of continental breakup, *Tectonophysics,* **716,** 130–148,

Rawlinson, N. & Sambridge, M. 2005. The fast marching method: an effective tool for tomographic imaging and tracking multiple phases in complex layered media, *Explor. Geophys.,* **36,** 341–350.

Ritsema, J. & Allen, R. 2003. The elusive mantle plume, *Earth planet. Sci. Lett.,* **207,** 1–12.

Ryberg, T., Brauer, B. & Weber, M.H. 2016a. Upper mantle structure at Walvis Ridge from *Pn* tomography, *Tectonophysics,* **716,** doi:10.1016/j.tecto.2016.08.009.

Ryberg, T., Geissler, W.H., Jokat, W. & Pandey, S. 2017. Uppermost mantle and crustal structure at Tristan da Cunha derived from ambient seismic noise, *Earth planet. Sci. Lett.,* **471,** 117–124.

Ryberg, T., Haberland, C., Green, R.G. & Sens-Schönfelder, Ch. 2021. A fast GUI based tool for group velocity analysis of surface waves, *Seismol. Res. Lett.,* **92,** 2640–2646.

Ryberg, T., Haberland, C., Haberlau, T., Weber, M., Bauer, K., Behrmann, J.H. & Jokat, W., 2015. Crustal structure of northwest Namibia: evidence for plume-rift-continent interaction, *Geology,* **43,** 739–742.

Ryberg, T., Muksin, U. & Bauer, K. 2016b. Ambient seismic noise tomography reveals a hidden caldera and its relation to the Tarutung pull-apart basin at the Sumatran Fault Zone, Indonesia, *J. Volc. Geotherm. Res.,* **321,** 73–84.

Sabra, K.G., Gerstoft, P., Roux, P., Kuperman, W.A. & Fehler, M.C. 2005. Surface wave tomography from microseisms in Southern California, *Geophys. Res. Lett.,* **32,** doi:10.1029/2005GL023155.

Schlömer, A., Geissler, H.W., Jokat, W. & Jegen, M. 2017. Seismicity in the vicinity of the Tristan da Cunha hotspot: particular plate tectonics and mantle plume presence, *J. geophys. Res.,* **122,** 10 427–10 439.

Schneider, G. *et al.* 2008. *The Roadside Geology of Namibia,* Vol. **IX,** 2nd edn, 294pp., Borntraeger Gebrueder.

Scholte, J.G. 1947. The range and existence of Rayleigh and Stoneley waves, *Geophys. J. Int.,* **5,** 120–126.

Schuster, G.T. 2009. *Seismic Interferometry.* Cambridge Univ. Press.

Sebai, A., Stutzmann, E., Montagner, J.-P., Sicilia, D. & Beucler, E., 2006. Anisotropic structure of the African upper mantle from Rayleigh and Love wave tomography, *Phys. Earth planet. Inter.,* **155,** 48–62.

Shapiro, N.M., Campillo, M., Stehly, L. & Ritzwoller, M.H. 2005. High-resolution surface wave tomography from ambient seismic noise, *Science,* **307,** 1615–1618.

Wessel, P. & Smith, W. 1995. New version of the Generic Mapping Tools released, *EOS, Trans. Am. Geophys. Un.,* **76,** 329.

Wessel, P. & Smith, W. 1998. New, improved version of the Generic Mapping Tool released, *EOS, Trans. Am. Geophys. Un.,* **79,** 579.

Wolf, F.N., Lange, D., Dannowski, A., Thorwart, M., Crawford, W., Wiesenberg, L., Grevemeyer, I. & Kopp, H., and the AlpArray Working Group, 2021. 3D crustal structure of the Ligurian Basin revealed by surface

wave tomography using ocean bottom seismometer data, *Solid Earth,* **12,** 2597–2613.

Yamaya, L., Mochizuki, K., Akuhara, T. & Nishida, K. 2021. Sedimentary structure derived from multi-mode ambient noise tomography with dense OBS network at the Japan Trench. *J. geophys. Res.,* **126,** e2021JB021789, doi:10.1029/2021JB021789.

Yao, H., Gouédard, P., Collins, J.A., McGuire, J.J. & van der Hilst, R.D., 2011. Structure of young East Pacific Rise lithosphere from ambient noise correlation analysis of fundamental- and higher-mode Scholte-Rayleigh waves, *C.R. Geosci.,* **343,** 571–583.

Yuan, X., Heit, B., Brune, S., Steinberger, B., H.Geissler, W., Jokat, W. & Weber, M. 2017. Seismic structure of the lithosphere beneath NW Namibia: impact of the Tristan da Cunha mantle plume. *Geochem. Geophys. Geosyst.,* **18,** 125–141.

Zha, Y., Webb, S.C., Wei, S.S., Wiens, D.A., Blackman, D.K., Menke, W.H., Dunn, R.A. & Conders, J.A. 2014. Upper mantle shear velocity structure beneath the Eastern Lau Spreading Center from OBS ambient noise tomography, *Earth planet. Sci. Lett.,* **408,** 194–206.